RESEARCH ARTICLE SUMMARY

NEUROIMMUNOLOGY

Group 2 innate lymphoid cells promote inhibitory synapse development and social behavior

Jerika J. Barron, Nicholas M. Mroz, Sunrae E. Taloma, Madelene W. Dahlgren, Jorge F. Ortiz-Carpena, Matthew G. Keefe, Caroline C. Escoubas, Leah C. Dorman, Ilia D. Vainchtein, Pailin Chiaranunt, Maya E. Kotas, Tomasz J. Nowakowski, Kevin J. Bender, Ari B. Molofsky*, Anna V. Molofsky*

INTRODUCTION: The innate immune system monitors and promotes healthy organ development, including that of the brain. Immune dysfunction in early life is implicated in neurodevelopmental and psychiatric disorders. In early life, innate immune cells, such as macrophages and innate lymphoid cells (ILCs), dominate responses. Therefore, ILCs are particularly relevant to processes that occur before the maturation of adaptive immune cells such as T and B cells. Group 2 ILCs (ILC2s) are a subset of ILCs that mediate allergic immune responses but are also increasingly implicated in tissue development, remodeling, and homeostasis. ILC2s produce several cytokines that mediate these remodeling responses, including interleukin-13 (IL-13), which signals through a heterodimeric receptor encoded by the *Il4ra* and *Il13ra1* genes. Although the impact of cytokines on immune cells is extensively studied, less is known about how they regulate tissue-resident cells, including neurons.

Neurons in the developing brain remodel trillions of synaptic connections to establish the mature neural circuits that are critical for brain function. There are two major synapse types in the brain. Excitatory synapses encode information and make long-range connections throughout the central nervous system, signaling via the neurotransmitter glutamate. By contrast, inhibitory synapses are formed by interneurons that act locally to tune neural circuit excitability and improve data fidelity, acting largely via the neurotransmitter γ-aminobutyric acid (GABA). Defining how innate immunity affects the development of these synapse types may yield insights into how immune signaling influences brain function.

RATIONALE: We previously found that the cytokine IL-33, a regulator of type 2 allergic immune responses, directly and indirectly regulates brain excitatory synapses. In this work, to more broadly examine the role of type 2 immunity in brain development, we defined the role of ILC2s and their effector cytokine IL-13 on the development of inhibitory and excitatory neuronal synapses in the developing cortex of mice. We also examined the impact of this pathway on adult behaviors.

RESULTS: Using single-cell RNA sequencing of the developing mouse brain meninges, we observed that innate lymphocytes outnumbered adaptive lymphocytes and included a large population of ILC2s. From flow cytometry of cells from the brain of mice that report endogenous cytokine levels, we found that ILC2s produced a wave of type 2 cytokines between postnatal days 5 and 22, which included IL-13 and IL-5. By contrast, adaptive CD4 T cells expressed minimal IL-13 and IL-5 during this developmental window. To determine the impact of ILC2s on brain development, we constitutively and selectively ablated ILC2s by expression of diphtheria toxin in cells expressing *Il5* (ΔILC2 mice). Using protein immunostaining and slice electrophysiology, we observed a decrease in inhibitory synapses in somatosensory and prefrontal cortices of ΔILC2 mice at P15 but not in adulthood. By contrast, mice that received donor ILC2s delivered intracerebroventricularly had more inhibitory synapses compared with vehicle-injected littermates. The IL-4/13 receptor *Il4ra* was expressed both in microglia and in neurons in the developing cortex. Deletion of either *Il4ra* globally or specifically in inhibitory interneurons but not in microglia phenocopied the inhibitory synapse deficits seen in ΔILC2 mice. Conversely, local injection of recombinant IL-13 was sufficient to increase inhibitory synapses. Throughout the perturbations described above, excitatory synapses were unchanged. Single-nucleus RNA sequencing of cortical inhibitory neurons after IL-13 injection revealed changes in genes linked to neuronal development and neuronal signaling in several interneuron subsets but no induction of canonical markers of type 2 immune activation. ΔILC2 mice, as well as mice that lacked *Il4ra* in interneurons, had impaired social interaction in the three-chamber social preference test, with no deficits in memory or cognition.

CONCLUSION: Our study identifies a role for ILC2s in promoting inhibitory synapse formation, thus establishing these cells as important regulators of brain development. Our finding that IL-13 signals directly to interneurons during development suggests a potential mechanism through which immune signals in early life can lead to long-lasting impacts on brain function and behavior. These data are consistent with an emerging body of literature showing that cytokines can signal directly to neurons, thereby acting as neuromodulators sensitive to the immune environment during critical periods of brain development. ■

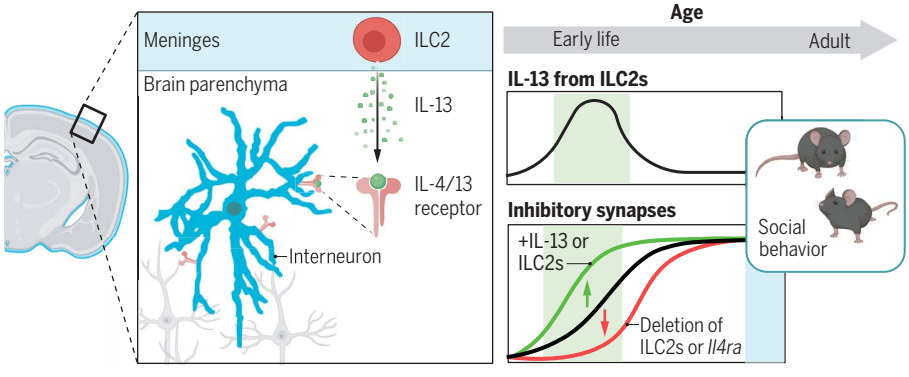

ILC2s promote early-life inhibitory synapse development and social behavior. Immune cells known as ILC2s located in the meningeal linings of the brain produce the cytokine IL-13 in early life to promote inhibitory synapse formation by interneurons, which are important regulators of brain development and function. Eliminating components of this pathway leads to impaired social behavior in adult mice. On the right, the green and blue shaded regions indicate the peak of IL-13 production and the age of behavioral assessments, respectively. [Figure created with BioRender.com]

The list of author affiliations is available in the full article online.
*Corresponding author. Email: anna.molofsky@ucsf.edu (A.V.M.); ari.molofsky@ucsf.edu (A.B.M.)
Cite this article as J. J. Barron *et al.*, *Science* **386**, eadi1025 (2024). DOI: 10.1126/science.adi1025

READ THE FULL ARTICLE AT
https://doi.org/10.1126/science.adi1025

RESEARCH ARTICLE

NEUROIMMUNOLOGY

Group 2 innate lymphoid cells promote inhibitory synapse development and social behavior

Jerika J. Barron[1,2], Nicholas M. Mroz[2,3], Sunrae E. Taloma[4,5,6], Madelene W. Dahlgren[3,7], Jorge F. Ortiz-Carpena[3], Matthew G. Keefe[1,8], Caroline C. Escoubas[1], Leah C. Dorman[1,9], Ilia D. Vainchtein[1]†, Pailin Chiaranunt[1,3], Maya E. Kotas[10], Tomasz J. Nowakowski[1,11,12], Kevin J. Bender[5,6], Ari B. Molofsky[3]*, Anna V. Molofsky[1,5]*

The innate immune system shapes brain development and is implicated in neurodevelopmental diseases. It is critical to define the relevant immune cells and signals and their impact on brain circuits. In this work, we found that group 2 innate lymphoid cells (ILC2s) and their cytokine interleukin-13 (IL-13) signaled directly to inhibitory interneurons to increase inhibitory synapse density in the developing mouse brain. ILC2s expanded and produced IL-13 in the developing brain meninges. Loss of ILC2s or IL-13 signaling to interneurons decreased inhibitory, but not excitatory, cortical synapses. Conversely, ILC2s and IL-13 were sufficient to increase inhibitory synapses. Loss of this signaling pathway led to selective impairments in social interaction. These data define a type 2 neuroimmune circuit in early life that shapes inhibitory synapse development and behavior.

The innate immune system monitors and promotes healthy organ development, including in the brain. Conversely, immune dysfunction by means of maternal immune activation or early life perturbations is implicated in neurodevelopmental and psychiatric disorders (*1*, *2*). Because these immune perturbations are transient, they are potentially consistent with a large body of data that suggests that perturbations in neural circuit maturation during key developmental windows can result in long-lasting changes in adult behavior (*3*–*5*). For example, an increase in the balance of neuronal excitation to inhibition (E/I) was proposed to underlie some disorders of neurodevelopment, including autism spectrum disorder (*6*). E/I imbalance can occur through multiple mechanisms, including alterations in excitatory or inhibitory neuronal numbers, synapses, and activity. However, the role of inhibitory interneurons may be particularly critical (*7*). Although inhibitory interneurons are a minority of the cortical neuronal population (~20%), they are dynamic modulators of neural circuit function that optimize signal-to-noise ratios and synchronize activity within and between brain regions (*8*). They are also altered in the context of immune activation (*9*) and may be particularly sensitive to environmental inputs (*10*). Thus, defining the immune signaling circuits that shape interneurons and inhibitory synapses may provide insights into basic mechanisms of neurodevelopment that may be affected in neurodevelopmental disorders.

Innate immune responses are dominant in early life and mediated by immune cells such as macrophages and innate lymphoid cells (ILCs), which are deposited in tissues during embryogenesis and early postnatal life. As such, innate immune responses may have a particular impact on tissue development, before the full maturation and expansion of adaptive immunity, which includes B and T lymphocytes. ILCs are the most recently discovered member of the innate immune arsenal (*11*, *12*). Their subtypes closely mirror the types of helper T lymphocytes that expand later in life (i.e., type 1, type 2, type 3/17). Unlike many T cells, ILCs produce cytokines within hours and in response to local tissue cues, rather than in response to specific antigens. Both adaptive and innate lymphocytes and their cytokines affect adult mouse behavior and cognition (*13*–*19*), which raises the question of whether some of these effects may occur during development and, if so, whether subsets of innate lymphocytes mediate these phenotypes.

Group 2 ILCs (ILC2s) are a subset of ILCs that are implicated in type 2 immune responses. ILC2s are dominant producers of effector cytokines, such as interleukin-13 (IL-13), in response to allergic immune activation. ILC2 precursors seed many peripheral organs during late fetal development in the mouse, but most ILC2 expansion in those tissues occurs during the early postnatal window concurrent with the acquisition of tissue-specific signatures (*20*). Type 2 immunity is critical to limiting infection by parasitic helminths, promoting tissue repair in injury, and driving allergic pathology (*21*) but also has emerging roles in tissue development and remodeling (*22*, *23*). In the nervous system, ILC2s promote repair after spinal cord injury (*24*). Within the brain parenchyma, the type 2 immune activator IL-33 signals to microglia to drive excitatory synaptic remodeling (*25*–*28*), which implicates aspects of type 2 immunity in neural circuit development. However, the kinetics of the ILC2 population and expansion in the nervous system, whether they produce effector cytokines, and whether those cytokines affect brain development and function are unknown. In this work, we investigated the impact of ILC2s and IL-13 signaling on synaptic development and behavior in mice using cell type–specific depletion, cell transfers, and cytokine loss- and gain-of-function approaches.

Results

Meningeal group 2 innate lymphocytes expand and produce IL-13 in early life

The central nervous system (CNS) immune environment is composed of cells within the brain parenchyma (primarily microglia) as well as in the brain borders, which include the meninges, perivascular spaces, and choroid plexus. These border regions contain a full complement of immune cell types, including macrophages, dendritic cells, and innate and adaptive lymphocytes, that mirror tissue immune niches in other organs (*29*, *30*). To define the immune environment of the developing brain meninges during synaptogenesis, we performed single-cell RNA sequencing (scRNA-seq) of the cranial meninges of mice on postnatal day 14 (P14) (Fig. 1A). At this age, lymphocytes have expanded sufficiently to enable us to capture a diversity of immune cell types within this early life window. To capture rarer cell populations and their supporting stroma, we enriched by cell sorting for lymphocytes and stromal cells in addition to the total cell isolation (fig. S1A). We recovered 12,544 cells for downstream unsupervised clustering analysis (Fig. 1B and fig. S1, B and C). We observed a full complement of immune cell types, including myeloid and lymphoid

[1]Department of Psychiatry and Behavioral Sciences–Weill Institute for Neurosciences, University of California, San Francisco, San Francisco, CA 94158, USA. [2]Biomedical Sciences Graduate Program, University of California, San Francisco, San Francisco, CA 94158, USA. [3]Department of Laboratory Medicine, University of California, San Francisco, San Francisco, CA 94158, USA. [4]Neuroscience Graduate Program, University of California, San Francisco, San Francisco, CA 94158, USA. [5]Kavli Institute for Fundamental Neurosciences, University of California, San Francisco, San Francisco, CA 94158, USA. [6]Department of Neurology, University of California, San Francisco, San Francisco, CA 94158, USA. [7]Lung Biology, Department of Experimental Medical Science, Lund University, Lund, Sweden. [8]Developmental and Stem Cell Biology Graduate Program, University of California, San Francisco, San Francisco, CA 94158, USA. [9]Chan-Zuckerberg Biohub, San Francisco, CA 94158, USA. [10]Division of Pulmonary, Critical Care, Allergy and Sleep Medicine, Department of Medicine, University of California, San Francisco, San Francisco, CA 94158, USA. [11]Department of Neurological Surgery, University of California, San Francisco, San Francisco, CA 94158, USA. [12]Department of Anatomy, University of California, San Francisco, San Francisco, CA 94158, USA.
***Corresponding author. Email: anna.molofsky@ucsf.edu (A.V.M.); ari.molofsky@ucsf.edu (A.B.M.)**
†Present address: Janssen Research & Development, Johnson & Johnson, San Diego, CA 92121, USA.

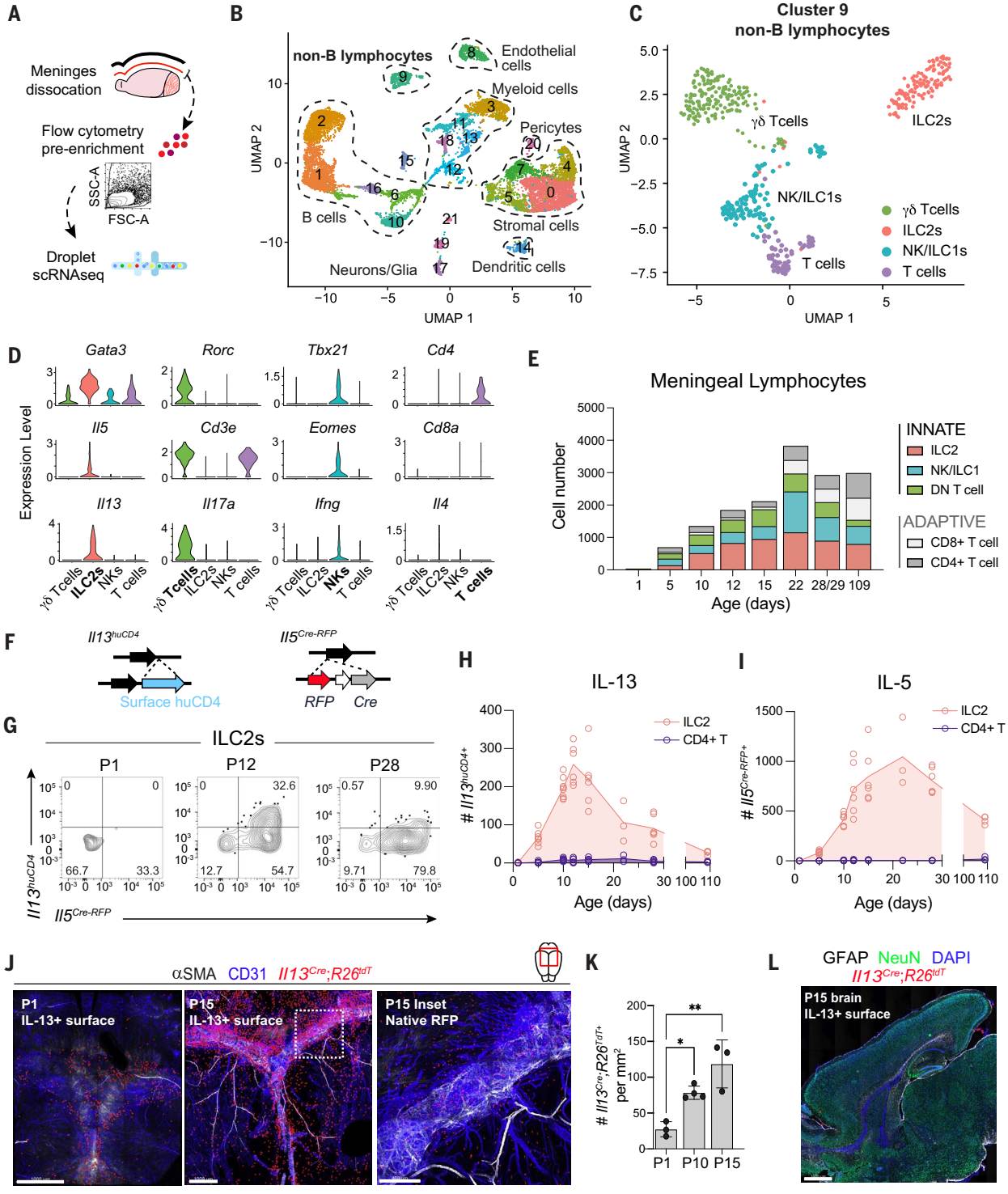

Fig. 1. Meningeal group 2 innate lymphocytes expand and produce IL-13 in early life. (**A**) Schematic of P14 cranial meninges isolation for flow cytometry and scRNA-seq. (**B**) Unsupervised clustering [uniform manifold approximation and projection (UMAP)] of 12,544 cells from P14 meninges (enriched for stromal cells and nonmyeloid immune cells) pooled from both sexes to obtain two replicates per genotype for *Il33*$^{mcherry/+}$ control (five female and seven male mice) and *Il33*$^{mcherry/mcherry}$ knockout (seven female and eight male mice). Cell-type assignments were based on marker-gene expression. See fig. S1, A to D, for flow cytometry gating, quality control metrics, and cell-type assignment. See data S1 for a list of cluster-defining genes. (**C**) Subclustering of non-B lymphocytes from (B), including T cells and ILCs (cluster 9; 477 cells). See fig. S1E and data S2 for cluster-defining genes. (**D**) Expression of lineage-defining and effector genes in non-B lymphocytes from (C). (**E**) Quantification by flow cytometry of innate and adaptive lymphocytes in the meninges by total cell number. The number of biological replicates per age are as follows: P1, *n* = 3 (two mice pooled per replicate); P5, *n* = 8 (two mice pooled per replicate); P10, *n* = 8; P12, *n* = 6; P15, *n* = 6; P22, *n* = 3; P28 or P29, *n* = 6; and P109 (adult), *n* = 4. See fig. S2B for gating strategy. DN T cell, double negative T cell. (**F**) Schematics depicting cytokine reporter constructs in relation to their endogenous murine loci. Note that *Il5*$^{Cre-RFP}$ leads to loss of function of the endogenous locus, whereas *Il13*^{huCD4}

is inserted into the 3′ untranslated region and preserves gene expression. *huCD4*, human CD4. (**G**) Representative flow plots showing expression of IL-5 (*Il5*$^{Cre\text{-}RFP}$) and IL-13 (*Il13*^{huCD4}) within *Arg1*$^{YFP+}$ meningeal ILC2s at select developmental time points (P1, P12, and P28), as quantified in (H) and (I). The gating strategy that was used to identify ILC2s is shown in fig. S2B. (**H**) Number of IL-13–expressing meningeal ILC2s and CD4$^+$ T cells over development (number of *Il13*$^{huCD4+}$*Arg1*$^{YFP+}$ ILC2s or *Il13*$^{huCD4+}$CD3$^+$CD4$^+$ T cells per mouse meninges). The number of biological replicates per age are as follows: P1, *n* = 3 (two mice pooled per replicate); P5, *n* = 8 (two mice pooled per replicate); P10, *n* = 8; P12, *n* = 6; P15, *n* = 6; P22, *n* = 3; P28 or 29, *n* = 6; and P109, *n* = 4. (**I**) Number of IL-5–expressing meningeal ILC2s and CD4$^+$ T cells over development (number of *Il5*$^{RFP+}$*Arg1*$^{YFP+}$ ILC2s or *Il5*$^{RFP+}$CD3$^+$CD4$^+$ T cells per mouse meninges). Biological replicates per age are as follows: P1, *n* = 3 (two mice pooled per replicate); P5, *n* = 8 (two mice pooled per replicate); P10, *n* = 8; P12, *n* = 6; P15, *n* = 6; P22, *n* = 3; P28 or 29, *n* = 6; and P109, *n* = 4. (**J**) Confocal image and surface reconstruction of whole-mount dural meninges, highlighting IL-13 lineage-traced cells (red squares, *Il13*$^{Cre\text{-}YFP}$:*R26*^{TdTomato}), vasculature (CD31), and αSMA at ages P1 and P15. On the right, the P15 inset (magnified area of the white dashed box in middle image) shows native *Il13*$^{Cre\text{-}YFP/+}$:*R26*$^{TdTomato/+}$ signal. Scale bars are 1 mm (P1 and P15) and 400 μm (P15 inset). (**K**) Quantification of meningeal IL-13$^+$ cells (*Il13*$^{Cre\text{-}YFP}$:*R26*$^{TdTomato+}$) at P1, P10, and P15 normalized per tissue area (*n* = 3 or 4 mice per age). Data were analyzed by one-way analysis of variance (ANOVA) with Tukey's multiple comparisons test. (**L**) Representative confocal image of sagittal brain section from IL-13 lineage reporter (*Il13*$^{Cre\text{-}YFP}$:*R26*^{tdTomato}) at P15 showing absence of parenchymal labeling. Staining shows IL-13$^+$ cells (*Il13*$^{Cre\text{-}YFP}$:*R26*^{TdTomato}; indicated by red squares for visualization), GFAP$^+$ astrocytic brain borders, NEUN$^+$ neurons, and 4′,6-diamidino-2-phenylindole (DAPI). Scale bar is 1 mm. See full image and insets in fig. S5. For (H) and (I), data are means; for (K), data are means ± SD. Individual data points represent data for one mouse. **p* < 0.05; ***p* < 0.01.

cells, consistent with studies in mice at other ages (*31*–*35*) (Fig. 1B and fig. S1D).

Unlike the adult meninges, innate lymphocytes were more abundant than adaptive lymphocytes at this early age. Subclustering of non-B lymphocytes (cluster 9) revealed an abundance of ILC2s (*Cd3e*$^-$, *Gata3*$^+$) and innate-like γδ T cells (*Cd3e*$^+$, *Rorc*$^+$), as well as smaller populations of natural killer (NK) cells (*Cd3e*$^-$, *Tbx21*$^+$, *Eomes*$^+$) and group 1 innate lymphoid cells (ILC1s) (*Cd3e*$^-$, *Tbx21*$^+$, *Eomes*$^-$; Fig. 1, C and D, and fig. S1E). By contrast, adaptive immune cells such as CD4$^+$ T cells (*Cd3e*$^+$, *Cd4*$^+$) were relatively rare. Our samples included mice deficient for the stromal cytokine IL-33, a regulator of synaptic development (*25*, *36*) and an activator of ILC2s; therefore, we examined its expression and impact on lymphocytes. IL-33 expression was enriched in meningeal fibroblasts (fig. S1F), which suggests that they may be a relevant meningeal source that is discrete from glial and neuronal IL-33 sources in the brain parenchyma. However, IL-33 deficiency did not reduce meningeal ILC2 numbers and had only modest effects on activation markers, including *Il13*, *Areg*, and *Cxcl2* (fig. S1, C and G). These data suggest that IL-33 is only partly responsible for ILC2 developmental expansion and activation, consistent with findings from other studies in developing lung and skin (*37*–*39*).

To assess the kinetics of meningeal lymphocyte expansion during postnatal development, we performed flow cytometry (ages P1 to P109; Fig. 1E and fig. S2, A to D). We observed an early postnatal expansion of innate lymphocytes, such as ILC2s and innate-like T cells, the numbers of which peaked between P15 and P22 and were modestly reduced by adulthood. Innate lymphocytes were more abundant than adaptive lymphocytes throughout postnatal development until they reached a roughly equal proportion in adult meninges (Fig. 1E and fig. S2, C and D). Circulating ILC2s were detectable but extremely rare in the early postnatal blood, whereas meningeal ILC2 expansion resembled that in other organs such as the lung (fig. S2, E and F) (*20*), which suggests that ILC2s expanded locally in the meninges and elsewhere in early postnatal life.

We next examined the effector functions of innate lymphocytes during development. All meningeal innate lymphocyte subsets expressed canonical transcription factors and effector genes required for cytokine production, whereas T cells did not, as determined both by gene expression (Fig. 1D and fig. S1E) and at the protein level (fig. S3, A to C). This suggested that meningeal innate lymphocytes, but not adaptive T cells, were poised to produce cytokines during development. We quantified effector cytokine production by meningeal lymphocytes using cytokine reporter mice, which sensitively report endogenous cytokine production without the need for ex vivo stimulation (*40*, *41*). We found that ILC2s produced a wave of IL-13 and IL-5 type 2 cytokine activity between P5 and P22 (*Il13*^{huCD4};*Il5*$^{Cre\text{-}RFP}$; Fig. 1, F to I, and fig. S3, D, F, and G). By contrast, adaptive CD4$^+$ T cells expressed minimal IL-5 and IL-13 across postnatal development (Fig. 1, H and I, and fig. S3, E to G). We further examined this using cytokine staining after ex vivo lymphocyte stimulation, which confirmed that ILC2s had the capacity to produce IL-5 and IL-13 protein from P10 to P14, whereas CD4$^+$ T cells did not (fig. S3, H to J). To see whether this postnatal surge of cytokine production occurred broadly across lymphocyte subsets, we also examined a cytokine reporter for interferon-γ (IFN-γ), a cytokine associated with type 1 antiviral immune responses. Unlike IL-13 production by ILC2s, IFN-γ was tonically expressed by meningeal NK cells and ILC1s throughout development and without an early peak in yellow fluorescent protein (YFP) expression (*Ifng*^{YFP}; fig. S4, A to D). Thus, although multiple innate lymphocyte subsets can produce cytokines, we observed an early life developmental window during which ILC2s produced IL-13.

To assess potential local sources of IL-13 in the developing brain, we used an IL-13 lineage reporter (*Il13*$^{Cre\text{-}YFP}$;*R26*^{tdTomato}), which, unlike *Il13*^{huCD4}, permanently labels cells with a history of *Il13* expression. We observed substantial numbers of IL-13$^+$ cells in the developing brain meninges by confocal microscopy (Fig. 1J). These were rare shortly after birth but expanded during the first 2 weeks of life, localizing primarily to α–smooth muscle actin (αSMA)–rich adventitial regions around the dural sinus and other large vasculature (Fig. 1, J and K). By contrast, IL-13 lineage-tracked cells were nearly undetectable in the brain parenchyma (Fig. 1L and fig. S5, A and B). Meningeal IL-13 lineage-tracked cells were hematopoietic cells (CD45$^+$) and predominantly ILC2s (fig. S5C). Together, these results reveal an expansion of ILC2s and IL-13 production in the brain meninges in early life, raising the question of whether they affect concurrent brain development.

ILC2s increase cortical inhibitory synapse density during brain development

During the early postnatal period, excitatory and inhibitory synapses form and mature in the cortex, whereas ~12% of pyramidal neurons and ~30% of inhibitory interneurons undergo programmed cell death (*8*, *42*, *43*). To determine whether ILC2s affected these aspects of cortical circuit development, we used a well-characterized genetic deletion model to constitutively ablate ILC2s through expression of diphtheria toxin (DTA) in cells expressing *Il5*$^{Cre\text{-}RFP}$ (*Il5*$^{Cre\text{-}RFP/Cre\text{-}RFP}$;*R26R*$^{DTA/DTA}$), referred to hereafter as "ΔILC2" (Fig. 2A). This deletion strategy is specific to ILC2s in development (*40*, *41*, *44*, *45*), and when used for lineage tracing, the *Il5*$^{Cre\text{-}RFP}$ allele labeled meningeal ILC2s (fig. S6, A and B). Because the *Il5*$^{Cre\text{-}RFP}$ construct replaces the endogenous IL-5 locus, all experiments compared ΔILC2 mice with *Il5*$^{Cre\text{-}RFP/Cre\text{-}RFP}$ littermates (controls), and all animals were IL-5 deficient. This strategy led to an ~80% depletion of ILC2s without altering other lymphocyte subsets in the meninges (Fig. 2, B and C; gating strategy as in fig. S3A).

We quantified excitatory and inhibitory synapses in ΔILC2 mice during postnatal development by immunofluorescent imaging and colocalization analysis of pre- and postsynaptic

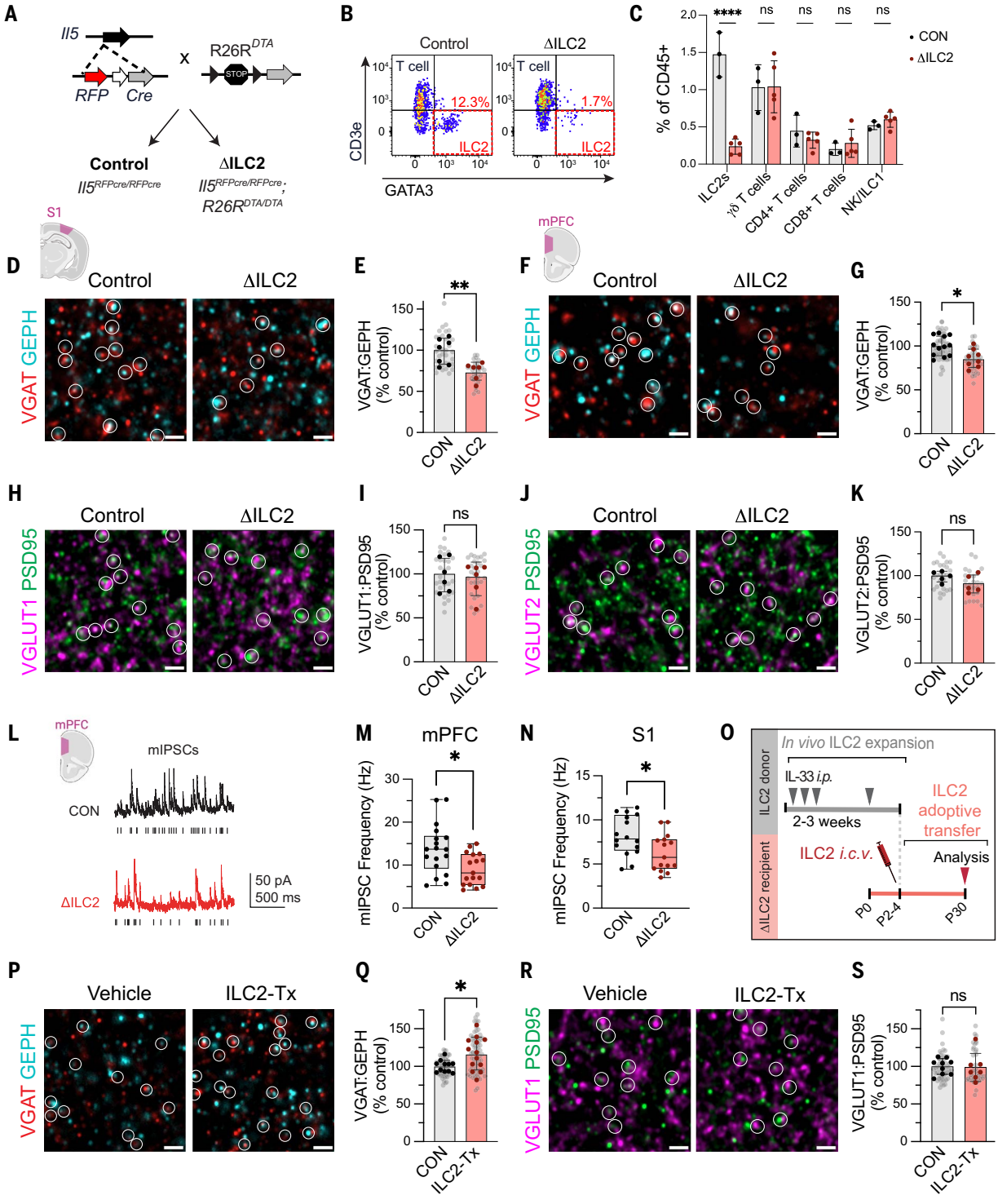

Fig. 2. ILC2s increase cortical inhibitory synapse density during brain development. (**A**) Schematic of "ILC2 depleter" mice (*Il5*$^{Cre\text{-}RFP/Cre\text{-}RFP}$:*R26R*$^{DTA/DTA}$, referred to as ΔILC2). All mice were homozygous for *Il5*$^{Cre\text{-}RFP}$; ΔILC2 mice were homozygous for *R26R*^{DTA}, whereas controls lacked the DTA allele. Littermates were used in all experiments unless otherwise noted. (**B**) Representative flow plots showing depletion of meningeal ILC2s (GATA3$^+$/CD3$^-$) in ΔILC2 mice compared with controls. Flow plots were pregated on live CD45$^+$CD11b$^-$CD19$^-$ cells (see fig. S3A for gating). (**C**) Quantification of lymphocyte subsets by flow cytometry in ΔILC2 or control mice at P15 as a percentage of viable CD45$^+$ cells (n = 3 controls, n = 5 ΔILC2 mice; points represent mice). See fig. S3A for gating. Data were analyzed by two-way ANOVA and Šídák's multiple comparisons test. (**D**) Representative images of inhibitory synapse immunofluorescent staining of presynaptic (VGAT) and postsynaptic (gephyrin, GEPH) markers in layer 4 somatosensory cortex (L4 S1) of control and ΔILC2 mice. Circles indicate examples of colocalized puncta. Scale bars are 2 μm. (**E**) Quantification of inhibitory VGAT$^+$GEPH$^+$ synapses in L4 S1 of control (CON) and ΔILC2 mice at P15 (n = 7 control, and n = 6 ΔILC2; three independent experiments). Data were analyzed by nested t test. (**F**) Representative images of inhibitory synapse immunofluorescent staining of VGAT and GEPH in L5b prefrontal cortex (mPFC) of control and ΔILC2 mice. Circles indicate examples of colocalized puncta. Scale bars are 2 μm.

(**G**) Quantification of inhibitory VGAT$^+$GEPH$^+$ synapses in mPFC of control and ΔILC2 mice at P15 (n = 12 control, and n = 8 ΔILC2; four independent experiments). Data were analyzed by nested t test. (**H**) Representative images of intracortical excitatory synapse immunofluorescent staining of presynaptic (VGLUT1) and postsynaptic (PSD95) markers in L4 S1 of control and ΔILC2 mice. Circles indicate examples of colocalized puncta. Scale bars are 2 μm. (**I**) Quantification of excitatory VGLUT1$^+$PSD95$^+$ synapses in L4 S1 of control and ΔILC2 mice at P15 (n = 6 control, and n = 6 ΔILC2; three independent experiments). Data were analyzed by nested t test. (**J**) Representative images of thalamocortical excitatory synapse immunofluorescent staining of presynaptic (VGLUT2) and postsynaptic (PSD95) markers in L4 S1. Circles indicate examples of colocalized puncta. Scale bars are 2 μm. (**K**) Quantification of excitatory VGLUT2$^+$PSD95$^+$ synapses in L4 S1 of control and ΔILC2 mice at P15 (n = 5 control, and n = 5 ΔILC2; two independent experiments). Data were analyzed by nested t test. (**L**) Representative traces of mIPSC recordings from layer 5 pyramidal neurons in mPFC acute brain slices. (**M**) Quantification of mIPSC frequency (Hz) in mPFC of control and ΔILC2 mice at P28 to P30 (n = 18 neurons from three control mice, and n = 17 neurons from three ΔILC2 mice; data points represent neurons). Data were analyzed by Mann-Whitney U test. (**N**) Quantification of mIPSC frequency (Hz) in S1 of control and ΔILC2 mice at P28 to P30 (n = 16 neurons from four control mice, and n = 15 neurons from four ΔILC2 mice; data points represent neurons). Data were analyzed by Mann-Whitney U test. (**O**) Schematic of experimental paradigm for in vivo expansion and activation of donor ILC2s and adoptive transfer of ILC2s into ΔILC2 recipient neonatal mice. i.c.v., intracerebroventricular; i.p., intraperitoneal. (**P**) Representative images of immunofluorescent staining of inhibitory VGAT$^+$GEPH$^+$ synapses in L4 S1 at P30 after neonatal transfer of ILC2s (ILC2-Tx) or vehicle. Circles indicate colocalized puncta. Scale bar is 2 μm. (**Q**) Quantification of inhibitory VGAT$^+$GEPH$^+$ synapses in L4 S1 at P30 after neonatal transfer of ILC2s (ILC2-Tx) or vehicle (n = 11 vehicle, and n = 13 ILC2-Tx; three independent experiments). Data were analyzed by nested t test. (**R**) Representative images of excitatory VGLUT1$^+$PSD95$^+$ synapses in L4 S1 at P30 after neonatal transfer of ILC2s (ILC2-Tx) or vehicle. Circles indicate colocalized puncta. Scale bars are 2 μm. (**S**) Quantification of inhibitory VGLUT1$^+$PSD95$^+$ synapses in L4 S1 at P30 after neonatal transfer of ILC2s (ILC2-Tx) or vehicle (n = 9 vehicle, and n = 7 ILC2-Tx; two independent experiments). Data were analyzed by nested t test. Data are means ± SD. Individual data points (dark color) represent data for one mouse, except in (M) and (N); gray data points represent technical replicates. Data are normalized to the mean of the control group within independent experiments, except in (C), (M), and (N). In (M) and (N), the center line represents the median, box limits are upper and lower quartiles, and whiskers are minimum and maximum values. ns, not significant; *p < 0.05; **p < 0.01; ****p < 0.0001. [Figure created in part with BioRender.com]

markers. Inhibitory synapses are defined here as the colocalization of the presynaptic marker vesicular γ-aminobutyric acid (GABA) transporter (VGAT) and the postsynaptic marker gephyrin. We observed a decrease in inhibitory synapses in ΔILC2 mice at P15, both in somatosensory cortex (S1, layer 4; Fig. 2, D and E, and fig. S6C) and in the medial prefrontal cortex (mPFC, L5b prelimbic area; Fig. 2, F and G). These reductions of inhibitory synapses were present across both superficial (L2/3) and deeper (L4) cortical layers (fig. S6D). Of note, these inhibitory deficits were no longer present by adulthood (fig. S6, E and F). We then quantified excitatory synapses, which comprise both intracortical synapses expressing vesicular glutamate transporter 1 (VGLUT1) and postsynaptic density protein 95 (PSD95), and thalamocortical synapses expressing vesicular glutamate transporter 2 (VGLUT2) and PSD95. In contrast to inhibitory synapses, excitatory synapses in this region were unaltered (Fig. 2, H and K, and fig. S6, G to K).

As an independent measure of inhibitory synaptic number and function, we performed whole-cell patch-clamp electrophysiologic recordings from excitatory neurons in the medial prefrontal cortex, as well as in the somatosensory cortex. These revealed fewer miniature inhibitory postsynaptic currents (mIPSCs) in both regions, consistent with a reduction in inhibitory synapse numbers, whereas amplitude, a measure of synaptic strength, was unchanged (Fig. 2, L to N, and fig. S7, A to D). Notably, although the number of VGAT:gephyrin synaptic contacts was most reduced at P15, we observed a reduction in mIPSCs at P30. This suggested that functional differences persisted at P30 that were not evident by immunolabeling for these two markers. The frequency and amplitude of miniature excitatory postsynaptic currents (mEPSCs) in L5b medial prefrontal cortex were not different (fig. S7, E and F). These data revealed a preferential impact of ILC2s on cortical inhibitory synapses during development, although further studies are needed to define the mechanisms and impact on synaptic function across development.

Inhibitory neurons can form synapses onto target neuron dendrites (axodendritic), cell bodies (axosomatic), or the axon initial segment (axoaxonic). Axodendritic synapses are the predominant synapse type in the cortex and likely represent the main synapse type that we quantified by colocalization of pre- and postsynaptic proteins. Axosomatic presynaptic contacts are formed primarily by parvalbumin-positive (PV$^+$) basket cells, and axoaxonic presynaptic contacts are made by PV$^+$ chandelier cells (*46*). We found that VGAT$^+$ presynaptic contacts were not altered at either sublocalization in ΔILC2 mice (fig. S8, A to D), which suggests a preferential impact of ILC2s on axodendritic inhibitory synapses. There was no difference in the number or distribution of inhibitory neurons across cortical layers as assessed by the pan-inhibitory neuron marker glutamate decarboxylase 67 (GAD67) or the subtype-specific markers PV and somatostatin (SST) at P15, a time point at which interneuron numbers have stabilized [fig. S8, E and F; (*42*, *43*)]. These data suggested that ILC2s promoted axodendritic inhibitory synapses but did not clearly implicate a specific interneuron subtype.

To determine whether ILC2s were sufficient to increase inhibitory synapses, we transferred ILC2s into neonatal ΔILC2 mice. ILC2s were harvested from donor mice that were pretreated with IL-33, which expands and primes ILC2s for IL-13 secretion (Fig. 2N and fig. S9, A to D) (*45*). To obtain enough cells for transfer, we used donor lung ILC2s and verified a similar level of cytokine activation in meningeal and lung ILC2s after IL-33 administration (fig. S9, C and D). Donor ILC2s were delivered by intracerebroventricular injection into ΔILC2 recipients between ages P2 and P4. We found that mice that received ILC2s had more inhibitory synapses at P30 compared with vehicle-injected littermates (Fig. 2, O to Q). However, because all recipients lacked ILC2s, we cannot definitively establish whether this represents a rescue or an increase. By contrast, excitatory synapses were not altered (Fig. 2, R and S). To determine the localization of donor ILC2s, we used the same strategy to deliver ILC2s isolated from *Il5*$^{Cre\text{-}RFP/+}$;*R26*$^{TdT/+}$ mice into wild-type recipients. Donor ILC2s were most abundant in the dural meninges, notably at the superior sagittal sinus, 2 days after transfer (P5) and decreased in number by P15 (fig. S9, E to G). ILC2s were occasionally observed in the brain parenchyma and in the lateral ventricles but were comparatively rare (fig. S9, H to K). ILC2 delivery did not lead to astrocyte or microglia reactivity in the S1 cortex at any time point (fig. S9, L to P). Taken together, these data showed that ILC2s were required for normal numbers of cortical inhibitory synapses during a period that closely follows their burst of IL-13 production and that local delivery of activated ILC2s into the brain is sufficient to increase postnatal inhibitory synapses.

IL-4/13 signaling to interneurons increases inhibitory synapse density during brain development

Given the temporal correlation between IL-13 production by ILC2s and their effect on inhibitory synapses, we assessed whether IL-13 could directly affect inhibitory synapses. IL-13 signals via a heterodimeric receptor that consists

of two subunits: IL-13 receptor subunit α1 (IL-13Rα1) and IL-4 receptor subunit α (IL-4Rα) [Fig. 3A; (47)]. Genetic loss of either obligate subunit eliminates IL-13 signaling. We found that global deficiency of the *Il4ra* subunit (*Il4ra*$^{-/-}$) phenocopied the reduction of inhibitory synapses seen in ILC2-deficient animals and did not alter excitatory synapse numbers (Fig. 3B and fig. S10A). Conversely, direct intracerebroventricular delivery of IL-13 at P14 was sufficient to increase inhibitory synapses within 20 hours and did not alter excitatory synapse numbers (Fig. 3C and fig. S10B). In adulthood, high systemic levels of IL-13 achieved by hydrodynamic gene delivery were not sufficient to increase inhibitory synapse density, which suggests that this effect is limited to a developmental window (fig. S10, C to E). These data demonstrated that IL-13/4 signaling during development promoted inhibitory, but not excitatory, synapse numbers.

To determine the cellular targets of IL-13 signaling in the developing cortex, we examined expression of the IL-13 receptor subunit *Il4ra*. *Il4ra* mRNA was detected throughout cortical layers with enrichment in L4 (fig. S10, F and G). Coimmunostaining revealed that microglia and myeloid cells (IBA1^{+}) expressed *Il4ra*, as did subsets of neurons (NEUN^{+}) and interneurons (*Vgat*$^{Cre+}$;*R26*$^{tdTomato+}$; Fig. 3, D and E), in line with published datasets from the murine cortex (48). scRNA-seq of non-neuronal cells in the developing cortex (49) and our meningeal scRNA-seq dataset confirmed expression of the receptor in myeloid cells, including microglia and meningeal macrophages (fig. S10, H and I). Therefore, both neurons and myeloid cells could be relevant cellular targets of IL-13 signaling during development.

Microglia expressed cell surface IL-4Rα and had a robust transcriptional response to exogenous IL-13 in vivo (fig. S11, A and B). To determine whether microglia or macrophages might mediate the effect of IL-13 on inhibitory synapses, we conditionally deleted *Il4ra* in these cell types by crossing *P2ry12*^{CreERT} or *Cx3cr1*^{CreERT} mice with those carrying the *Il4ra*^{flox} gene (50). There was no impact on inhibitory synapse numbers after conditional deletion of the IL-4/13 receptor in microglia or in myeloid cells (fig. S11, C to H). Thus, IL-13 signaling to myeloid cells was dispensable for inhibitory synapse development.

By contrast, we observed a decrease in inhibitory synapses when we conditionally deleted *Il4ra* from GABA-producing (GABAergic) inhibitory neurons (Fig. 3F and fig. S12, A and B; *Vgat*$^{Cre/+}$:*Il4ra*$^{flox/flox}$, referred to hereafter as "interneuron *Il4ra* cKO"). Excitatory synapses were not altered in these mice. We validated the specificity of *Vgat*^{Cre} to interneurons using a lineage trace reporter (fig. S12, C and D) and verified conditional gene deletion by polymerase chain reaction (PCR) and single-molecule fluorescence in situ hybridization (smFISH) (fig. S12, E to H). As previously reported, the presence of the *Cre* allele on its own had no effect on synapse numbers (fig. S12I). Analysis of cortical inhibitory synapses in adulthood showed no difference (fig. S12K). Deletion of *Il4ra* with a pan-neuronal transgenic Cre (*Syn1*^{Cre};*Il4ra*$^{flox/flox}$) showed a trend toward fewer inhibitory synapses (fig. S12, L and M). These data were consistent with IL-13 acting on receptors expressed by inhibitory neurons to promote postnatal inhibitory synapse formation.

We next examined which interneuron subsets might respond to IL-13. We used mice expressing a nuclear reporter construct [*GFP*^{Nuc} (51); GFP, green fluorescent protein] to enrich for GABAergic neuronal nuclei from P15 *Vgat*$^{Cre/+}$:*GFP*$^{Nuc/+}$ mice 4 hours after injection with IL-13 or saline and performed droplet-based single-nucleus RNA sequencing (snRNA-seq; Fig. 3G and fig. S13A). We obtained 16,104 inhibitory neuronal nuclei for downstream analysis (fig. S13, B and C). Unsupervised clustering revealed the expected major cardinal classes of cortical inhibitory neurons: SST, PV, lysosome-associated membrane protein 5 (Lamp5), and vasoactive intestinal peptide (VIP) (Fig. 3H and fig. S13, D and E), which could be more finely subclustered as reported by other studies [fig. S13F; (48, 52)]. Broadly, SST, PV, and Lamp5 classes function in inhibition of circuits, whereas VIP promotes disinhibition, although there is also substantial heterogeneity within classes that is still being deciphered (46). We observed expression of the IL-13 receptor subunits *Il4ra* and *Il13ra1* in multiple interneuron types, including SST, VIP, and PV clusters (Fig. 3I).

We analyzed differentially expressed genes (DEGs) in each broad cluster by treatment condition (Fig. 3, J and K, and fig. S13G). We observed the most DEGs in the SST, PV, and Lamp5 clusters, with very few in the VIP cluster. Interestingly, similar genes were up- and down-regulated across different interneuron clusters. For example, a comparison of PV and SST clusters showed up-regulation of the calcium channel *Cacna1a* and the Stat regulator *Ociad2* and down-regulation of the GABA transporter GAT-1 (*Slc6a1*) and the teneurins *Tenm1* and *Tenm2*. Pathway enrichment analysis of all up-regulated genes revealed changes in pathways associated with neuronal and synaptic function, rather than canonical pathways associated with IL-4/13 activation in immune cells, as we had observed in microglia (fig. S11B). These data suggested that IL-13 may induce a functional state change in multiple types of interneurons, rather than activating a single lineage-defined interneuron class. More broadly, it is consistent with the emerging view that some cytokines act as direct neuromodulators (53, 54).

ILC2s and IL-13 signaling to interneurons promote social behavior

Synaptic inhibition plays critical roles in tuning overall CNS network activity (8, 55) and can have long-lasting impacts on cognition and behavior (3–5). To determine the impact of ILC2s on behavior, we examined activity, anxiety, social preference and memory, object recognition and memory, and contextual fear memory in ΔILC2 mice and controls (age 2 to 3 months). Preference for social interaction was measured using Crawley's three-chamber assay. After chamber habituation, mice were allowed to explore the field, which contained a novel mouse under a wire cup in one chamber and an empty cup in the other. Whereas all mice spent a similar amount of time with the empty cup, ΔILC2 mice had a reduced preference for social interaction indicated by reduced social interaction time and discrimination index relative to controls (Fig. 4, A to C). These differences were not due to reductions in activity, as measured in both the three-chamber assay (Fig. 4D) and the open field test (fig. S14A). Preference for a novel versus familiar mouse was not altered 24 hours later (fig. S14, B and C). Other behavioral metrics were not altered, including novel object recognition, anxiety-like behavior in an elevated plus maze, and fear learning in a contextual fear-conditioning paradigm (fig. S14, D to I).

We next performed behavioral assays in mice with loss of *Il4ra* in interneurons. Similar to ΔILC2 mice, interneuron *Il4ra* cKO animals had a reduced preference for social interaction in the three-chamber assay relative to littermate controls (Fig. 4, E to G) and no differences in other behavioral measures (Fig. 4H and fig. S14, J to L). Thus, both ILC2 deficiency and loss of IL-13 signaling to interneurons preferentially affected social behavior. Overall, these data suggested that ILC2-derived IL-13 directly increased developmental inhibitory synapses through a presynaptic mechanism and promoted social interaction (table S1).

Discussion

Innate lymphocytes are emerging players in organ development and homeostasis (11). Our study establishes these cells as important regulators of brain development. We observed an expansion of innate lymphocytes in the early postnatal brain meninges and a peak of IL-13 production by meningeal ILC2s in early life, mirroring a similar wave of ILC2 expansion and activation in lung, skin, and intestine (20, 37). The cause of this early postnatal wave, and what makes it specific to ILC2 activation, remains to be determined. Although the microbiome is a potential candidate, ILC2 expansion and activation is largely microbiome-independent in tissues such as the skin, lung, and intestine (37), and the developmental surge of IL-13 production occurs preweaning, which is less

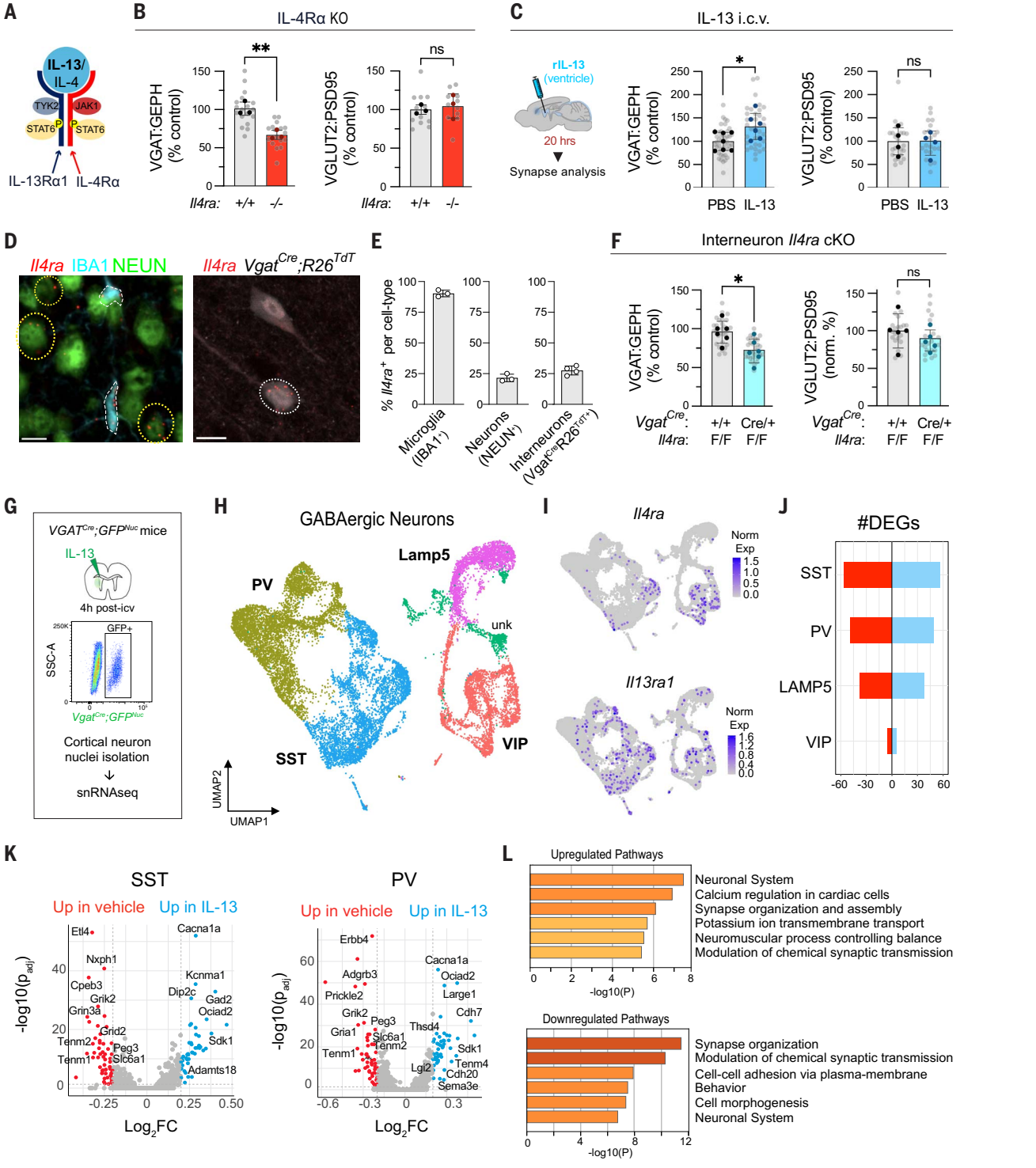

Fig. 3. IL-4/13 signaling to cortical interneurons increases inhibitory synapse density during brain development. (**A**) Schematic of the IL-4/13 receptor, which consists of the IL-13Rα1 and IL-4Rα subunits. (**B**) Quantification of inhibitory (VGAT$^+$GEPH$^+$) and excitatory (VGLUT2$^+$PSD95$^+$) synapses in *Il4ra*$^{+/+}$ and *Il4ra*$^{-/-}$ mice at P15 (n = 3 mice per group). Data were analyzed by nested t tests. See fig. S10A for representative images. (**C**) Quantification of inhibitory (VGAT$^+$GEPH$^+$) and excitatory (VGLUT2$^+$PSD95$^+$) synapses after intracerebroventricular (i.c.v.) injection of IL-13 (250 ng) or phosphate-buffered saline (PBS) at P15 (inhibitory: n = 7 control and n = 6 IL-13 mice; excitatory: n = 4 mice per group; two or three independent experiments). Data were analyzed by nested t tests. See fig. S10B for representative images. (**D**) Representative fluorescent in situ hybridization for *Il4ra* in the somatosensory cortex coimmunostained with cell-type markers. The left image shows colocalization of *Il4ra* transcript with IBA1$^+$ microglia (white dashed outline) or with NEUN$^+$ neurons (yellow dashed ovals). The right image shows colocalization of *Il4ra* transcript with an inhibitory interneuron reporter (*Vgat*$^{Cre/+}$;*R26*$^{tdTomato+}$; white dashed oval). Scale bars are 10 μm. (**E**) Quantification of *Il4ra*$^+$ cells from (D) as a percentage of each cell type in somatosensory cortex at P30 (n = 3 or 4 mice; data points represent mice). (**F**) Quantification of inhibitory (VGAT$^+$GEPH$^+$) and excitatory (VGLUT2$^+$PSD95$^+$) synapses in interneuron *Il4ra* interneuron cKO and control

mice at P30 (inhibitory: n = 6 mice per genotype; excitatory: n = 5 mice per genotype; two independent experiments). Data were analyzed by nested t tests. (**G**) Schematic of the snRNA-seq experiment analyzing inhibitory neuronal response to IL-13. *Vgat*$^{Cre/+}$;*GFP*^{Nuc} mice (age P15) were injected with vehicle or IL-13 (200 ng), and GFP$^+$ nuclei were isolated by flow sorting 4 hours later for 10X snRNA-seq. (**H**) Unsupervised clustering (UMAP) of 16,104 nuclei from P15 cortex after IL-13 or saline treatment (n = 4 mice; two replicates per condition, including one male and one female per condition). See fig. S13, A to E, and data S3 for flow gating, quality control metrics, and cell-type assignment. (**I**) Feature plots of the IL-13 receptor components *Il4ra* and *Il13ra1* across UMAP clusters showing normalized expression. Cells with expression have been brought to the front for visualization. (**J**) Number of up-regulated and down-regulated DEGs plotted by broad inhibitory neuron cell type from (H). (**K**) Volcano plots of SST (left) and PV (right) cluster DEGs with IL-13 versus vehicle treatment, showing log fold change ($\log_2$FC) in gene expression of IL-13 compared with vehicle, plotted against adjusted p value [$-\log10(p_{adj})$]. Thresholds are as follows: $\log_2$FC >0.2 and <−0.2, and adjusted p value <0.05 (see also data S5). (**L**) Metascape analysis of the top six up- or down-regulated pathways from all DEGS in IL-13–treated interneurons. Data are means ± SD. Individual data points (dark color) represent data for one mouse. In (B), (C), and (F), gray data points represent technical replicates, and data are normalized to the mean of the control group within independent experiments. ns, not significant; *p < 0.05; **p < 0.01.

consistent with a major shift in the microbiome. Regardless of the cause, it is interesting to speculate that this body-wide developmental activation of ILC2s in multiple tissues could help to synchronize development across organ systems, including the brain.

Alterations in neuronal inhibition have broad impacts, from preventing hyperexcitability and seizures to more complex effects on adult social behavior and cognition (*6*). Our work identified an immune mechanism that promotes synaptic inhibition in the developing brain. This ILC2–IL-13 neuroimmune circuit acted directly on inhibitory interneurons through a presynaptic mechanism. Interneurons represent a minority (~20%) of cortical neurons but are powerful and dynamic modulators of brain function (*8*). Our finding that IL-13 signaled directly to interneurons fits with an emerging body of literature demonstrating that cytokine receptor expression on neurons affects brain development and social behavior, including studies of the IL-17A pathway (*5*, *56*). Further, it is consistent with emerging work that shows direct cytokine signaling to inhibitory interneurons in the adult brain, including IFN-γ and IL-4 (*14*, *19*). Given that interneurons are morphologically, molecularly, and functionally diverse (*46*), determining whether specific interneuron subtypes respond to ILC2s and IL-13 is a key future direction.

Unlike previous studies, which have focused on T cells and adaptive immune responses, our data demonstrate that the innate type 2 signaling pathway mediated by ILC2s and IL-13 plays a role in the developing brain. This raises the question of whether this innate circuit may be relevant to prior phenotypes identified in mice with loss of IL-4/13 and IL-4 receptor signaling in adulthood (*16*, *19*, *57*–*60*), when adaptive T cells are more numerous. Although these and other studies have demonstrated that lymphocyte-derived cytokines affect the brain, these cells are largely outside the blood-brain barrier. Emerging data suggest that the blood-brain barrier is dynamic and permeable to many biologically active molecules (*61*). Further, pathways between associated skull bone marrow, meninges, and CNS cerebrospinal and interstitial spaces have recently been observed (*62*, *63*). Defining these doors into the CNS during development, and the routes through which cytokines reach the CNS parenchyma, is an essential future direction in understanding the brain-immune interface.

Ultimately, our findings raise the question of whether type 2 immune signals affect the human brain. Alterations in excitatory-inhibitory synaptic balance are implicated in disorders that include epilepsy, autism spectrum disorders, and schizophrenia (*1*). As such, altered type 2 immune tone by asthma, allergies, and parasitic infection might affect cognitive and social development in early life. For example, high parasite burden is a common feature of childhood in many parts of the world and is frequently associated with delays in learning and cognition (*64*, *65*). Although these phenotypes are likely multifactorial, it is possible that increased inhibition during sensitive periods of brain development contributes to negative cognitive outcomes in human populations. Conversely, given the emerging potential of immunotherapies in the treatment of diseases, type 2 immunomodulators might represent a previously unappreciated therapeutic direction for neurodevelopmental diseases by tuning inhibitory function. Directly examining how type 2 immune challenges affect brain development and defining the relevant variables that constrain these effects, such as age and sex, could therefore have major impacts on human health.

Materials and methods

Animal studies

All mouse strains were maintained in the University of California, San Francisco, specific pathogen–free facility, and all animal protocols were approved by Institutional Animal Care and Use Committee and Laboratory Animal Resource Center. Mice were housed in a 12-hour light-dark cycle. Adult mice were housed at a density of fewer than five mice per cage, and preweanling mice were housed with dams at a density of 12 or fewer per cage. Mice were euthanized in accordance with the American Veterinary Medical Association (AVMA) Guidelines on Euthanasia. Briefly, mice were deeply anesthetized and perfused transcardially with phosphate-buffered saline (PBS) and, if applicable, paraformaldehyde (PFA), as detailed further in the supplementary materials and Methods. Littermate controls were used for all experiments where feasible, and mice were backcrossed >10 generations on a C57BL/6 background unless otherwise indicated.

Meningeal isolation and scRNA-seq and analysis

The dural meninges was isolated from the dorsal skullcap using gentle scraping and pulled away in an intact sheet. For cell sorting before scRNA-seq, cells were enriched for lymphocyte and stromal populations by sorting CD45$^+$CD11b$^-$ and gp38$^+$CD31$^-$ populations, respectively, and pooling each of those populations to 25% of total cells, with 50% of all viable cells. Approximately 35,000 sorted cells of each sample were loaded per well of the Chromium Chip B (10X Genomics), and libraries were generated using the Single Cell 3′ reagent kit v3 (10X Genomics) according to the manufacturer's instructions. Sequenced samples were processed using the Cell Ranger 3.0.2 pipeline, aligned to the GRCm38 (mm10) mouse reference genome, and further analyzed using R (v 3.6.1) and Seurat (v 3.1.5) (*66*).

Neuronal snRNA-seq and analysis

Vgat^{Cre};*GFP*^{Nuc} mice were injected unilaterally with saline or IL-13 (200 ng) at P15. Four hours after injection, mice were perfused with ice-cold PBS, and sensory cortex was dissected from the ipsilateral hemisphere and snap frozen on dry ice. Nuclei were isolated by mechanical dissociation, then flow sorted for Hoechst$^+$ GFP$^+$ single nuclei. Then, 20,000 GFP$^+$ nuclei were loaded per well of the Chromium Next GEM Chip G (10X Genomics), and libraries were generated using the Next GEM Single Cell 3′ reagent kit v3.1 (10X Genomics). Sequenced samples were processed using CellRanger v7.0.1 and were aligned to mouse reference transcriptome mm10. CellRanger outputs were processed using Seurat.

Synaptic immunostaining and quantification

Mice were perfused transcardially with ice-cold PBS followed by 4% (weight/volume) PFA. Brains were postfixed in 4% PFA at 4°C for 4 to 5 hours and cryoprotected in 20% sucrose solution for a minimum of 2 days. Brains were flash frozen and sliced in 40-μm-thick coronal sections. Free-floating sections underwent antigen retrieval with 0.01 M sodium citrate pH 6 (95°C

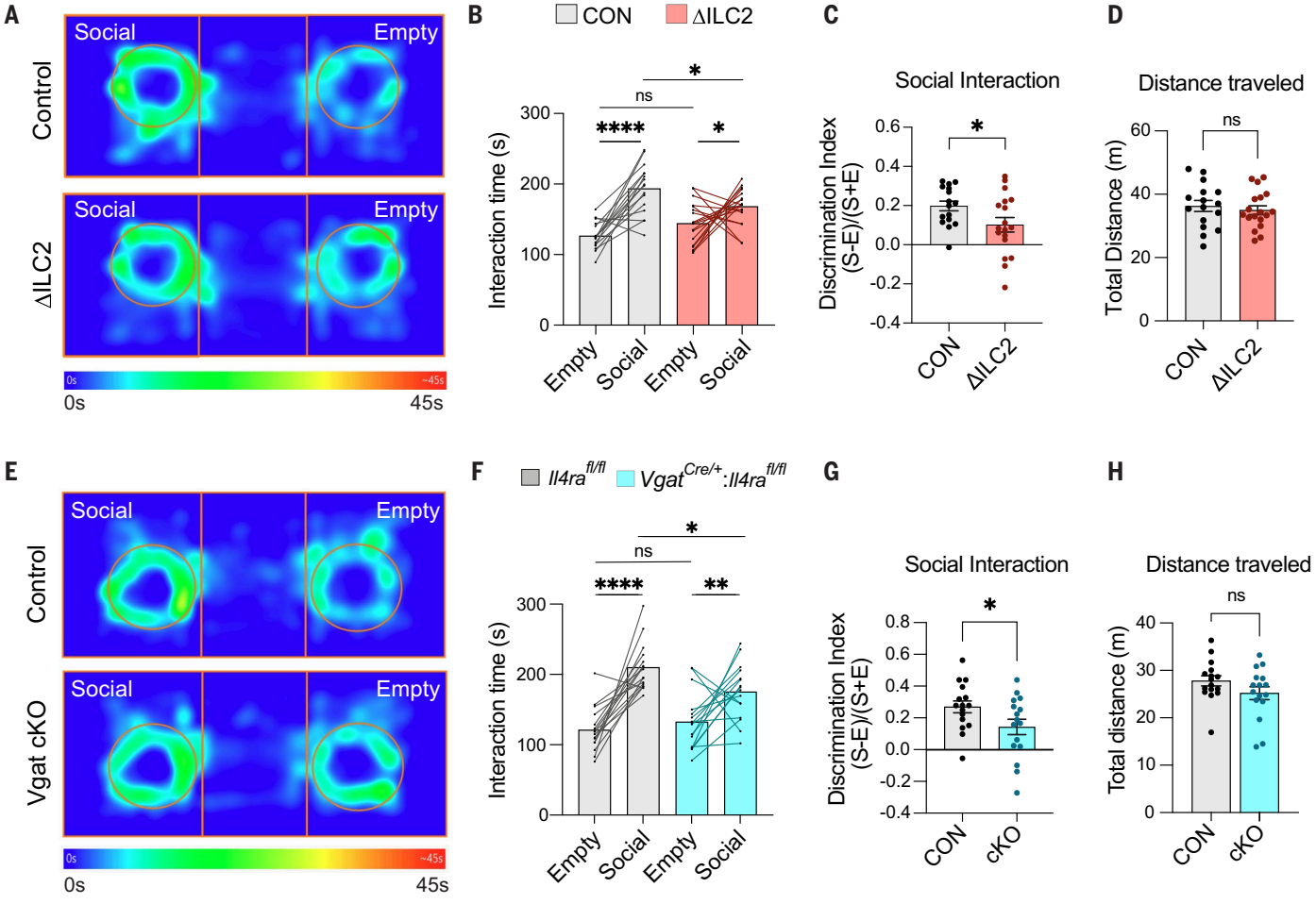

Fig. 4. ILC2s and IL-13 signaling to interneurons promote social behavior. (**A**) Representative group-averaged heatmaps of head tracking showing interaction time (seconds) with social or empty stimuli by control and ΔILC2 mice, revealing impaired social preference. (**B**) Interaction time spent with the empty versus social cup for control and ΔILC2 mice (n = 16 to 18 mice per genotype; three independent experiments). Data were analyzed by two-way ANOVA and Šídák's multiple comparisons test. (**C**) The social interaction discrimination index for control and ΔILC2 mice calculated as the difference in interaction time with the social (S) and empty (E) cup over total interaction time [(S − E)/(S + E)]. Data were analyzed by Welch's t test. (**D**) Total distance traveled during the three-chamber social interaction assay by control and ΔILC2 mice. Data were analyzed by Welch's t test. (**E**) Representative group-averaged heatmaps of head tracking showing interaction time with social or empty stimuli by control and interneuron *Il4ra* cKO mice. (**F**) Interaction time spent with the empty versus social cup for control and interneuron *Il4ra* cKO mice (n = 16 mice per genotype; two independent experiments). Data were analyzed by two-way ANOVA and Šídák's multiple comparisons test. (**G**) The social interaction discrimination index for control and interneuron *Il4ra* cKO mice calculated as the difference in interaction time with the social (S) and empty (E) cup over total interaction time [(S − E)/(S + E)]. Data were analyzed by Welch's t test. (**H**) Total distance traveled during the three-chamber social interaction assay by control and interneuron *Il4ra* cKO mice. Data were analyzed by Welch's t test. Data are means ± SEM or mean with lines connecting paired data for each mouse. Individual data points represent data for one mouse. ns, not significant;*p < 0.05; **p < 0.01; ****p < 0.0001.

for 10 min), followed by staining with primary and secondary antibodies. For synaptic puncta quantification, brain sections were imaged with a 63X/1.4 NA Plan-Apochromat oil-immersion objective. Single optical sections were acquired at a consistent depth of 5 μm below the surface. Analyses were conducted in layer 4 of S1 somatosensory cortex medial to the barrel field unless otherwise noted. For IL-13 intracerebroventricular injection experiments, the same region was quantified at ~100 to 250 μm from the injection site. The ImageJ2 plugin PunctaAnalyzer was used to quantify the numbers of synaptic puncta and the colocalization of presynaptic and postsynaptic marker channels. Puncta counts were normalized to the mean of controls within each experiment.

Quantification of meningeal lineage-traced cells

Whole-mounted meningeal tissues were imaged with a Nikon A1R laser scanning confocal microscope (405-, 488-, 561-, and 650-nm laser lines) using a 16X/0.8 NA Plan Apo or a 20X/0.95 NA XLUM Plan Apo water-immersion objective (512 resolution, 1 frame/s, Z step-size = 4 μm). Z stack images were rendered into three dimensions and quantitatively analyzed using Bitplane Imaris v9.5.1 software (Andor Technology PLC, Belfast, Northern Ireland). Three-dimensional reconstructions of tdTomato$^+$ cells were generated and quantified using the Imaris surface function on *Il13*- or *Il5*-tdTomato$^+$ cells with thresholds for tdTomato signal intensity, volume, sphericity, and/or 4′,6-diamidino-2-phenylindole (DAPI)–signal intensity, as described previously (*44*, *45*).

Slice preparation and patch-clamp electrophysiology

Mice were deeply anesthetized with isoflurane and euthanized. Then, 250-μm-thick coronal slices were prepared using a Leica VT1200 microtome. Recording electrodes contained cesium chloride or cesium methansulfonate intracellular solution. Recordings were performed in

voltage-clamp mode in the presence of artificial cerebrospinal fluid (aCSF) supplemented with tetrodotoxin (TTX). The experimenter was blinded to genotype.

ILC2 adoptive transfers

In vivo expansion and activation of ILC2s was performed in *Il5*$^{Cre\text{-}RFP/+}$;*R26*$^{TdT/+}$ mice with four 500-ng injections of recombinant carrier-free murine IL-33. Lung ILC2s were isolated by flow cytometry, and 20,000 cells (or saline control) were injected intracerebroventricularly into ILC2-deficient (ΔILC2) mice using a stereotaxic apparatus.

Behavioral assays

Experiments were conducted in 8- to 14-week-old mice. ILC2-deficient and control mice underwent a series of assays in order in three independent cohorts: open field test, novel object recognition, object place recognition, social interaction test, social recognition memory test, elevated plus maze, and contextual fear conditioning. Interneuron *Il4ra* conditional knockout and control mice underwent the same assays in order, except elevated plus maze, in two independent cohorts. Sociability and preference for social novelty were measured using Crawley's three-chamber test. Ovariectomized female mice were used as novel mice for testing social interaction and recognition. The experimenter was blinded to genotype throughout data collection and analysis.

REFERENCES AND NOTES

1. F. C. Bennett, A. V. Molofsky, The immune system and psychiatric disease: A basic science perspective. *Clin. Exp. Immunol.* **197**, 294–307 (2019). doi: 10.1111/cei.13334; pmid: 31125426
2. I. Knuesel *et al*., Maternal immune activation and abnormal brain development across CNS disorders. *Nat. Rev. Neurol.* **10**, 643–660 (2014). doi: 10.1038/nrneurol.2014.187; pmid: 25311587
3. S. H. Bitzenhofer, J. A. Pöpplau, M. Chini, A. Marquardt, I. L. Hanganu-Opatz, A transient developmental increase in prefrontal activity alters network maturation and causes cognitive dysfunction in adult mice. *Neuron* **109**, 1350–1364.e6 (2021). doi: 10.1016/j.neuron.2021.02.011; pmid: 33675685
4. L. Magno *et al*., Transient developmental imbalance of cortical interneuron subtypes presages long-term changes in behavior. *Cell Rep.* **35**, 109249 (2021). doi: 10.1016/j.celrep.2021.109249; pmid: 34133916
5. M. D. Reed *et al*., IL-17a promotes sociability in mouse models of neurodevelopmental disorders. *Nature* **577**, 249–253 (2020). doi: 10.1038/s41586-019-1843-6; pmid: 31853066
6. V. S. Sohal, J. L. R. Rubenstein, Excitation-inhibition balance as a framework for investigating mechanisms in neuropsychiatric disorders. *Mol. Psychiatry* **24**, 1248–1257 (2019). doi: 10.1038/s41380-019-0426-0; pmid: 31089192
7. A. Contractor, I. M. Ethell, C. Portera-Cailliau, Cortical interneurons in autism. *Nat. Neurosci.* **24**, 1648–1659 (2021). doi: 10.1038/s41593-021-00967-6; pmid: 34848882
8. G. Fishell, A. Kepecs, Interneuron types as attractors and controllers. *Annu. Rev. Neurosci.* **43**, 1–30 (2020). doi: 10.1146/annurev-neuro-070918-050421; pmid: 31299170
9. N. A. Vasistha *et al*., Maternal inflammation has a profound effect on cortical interneuron development in a stage and subtype-specific manner. *Mol. Psychiatry* **25**, 2313–2329 (2020). doi: 10.1038/s41380-019-0539-5; pmid: 31595033
10. L. J. Ansen-Wilson, R. J. Lipinski, Gene-environment interactions in cortical interneuron development and dysfunction: A review of preclinical studies. *Neurotoxicology* **58**, 120–129 (2017). doi: 10.1016/j.neuro.2016.12.002; pmid: 27932026
11. G. Gasteiger, X. Fan, S. Dikiy, S. Y. Lee, A. Y. Rudensky, Tissue residency of innate lymphoid cells in lymphoid and nonlymphoid organs. *Science* **350**, 981–985 (2015). doi: 10.1126/science.aac9593; pmid: 26472762
12. M. E. Kotas, R. M. Locksley, Why innate lymphoid cells? *Immunity* **48**, 1081–1090 (2018). doi: 10.1016/j.immuni.2018.06.002; pmid: 29924974
13. N. C. Derecki *et al*., Regulation of learning and memory by meningeal immunity: A key role for IL-4. *J. Exp. Med.* **207**, 1067–1080 (2010). doi: 10.1084/jem.20091419; pmid: 20439540
14. A. J. Filiano *et al*., Unexpected role of interferon-γ in regulating neuronal connectivity and social behaviour. *Nature* **535**, 425–429 (2016). doi: 10.1038/nature18626; pmid: 27409813
15. J. Kipnis, Multifaceted interactions between adaptive immunity and the central nervous system. *Science* **353**, 766–771 (2016). doi: 10.1126/science.aag2638; pmid: 27540163
16. T. M. Brombacher *et al*., IL-13-mediated regulation of learning and memory. *J. Immunol.* **198**, 2681–2688 (2017). doi: 10.4049/jimmunol.1601546; pmid: 28202615
17. M. Ribeiro *et al*., Meningeal γδ T cell-derived IL-17 controls synaptic plasticity and short-term memory. *Sci. Immunol.* **4**, eaay5199 (2019). doi: 10.1126/sciimmunol.aay5199; pmid: 31604844
18. K. Alves de Lima *et al*., Meningeal γδ T cells regulate anxiety-like behavior via IL-17a signaling in neurons. *Nat. Immunol.* **21**, 1421–1429 (2020). doi: 10.1038/s41590-020-0776-4; pmid: 32929273
19. J. Herz *et al*., GABAergic neuronal IL-4R mediates T cell effect on memory. *Neuron* **109**, 3609–3618.e9 (2021). doi: 10.1016/j.neuron.2021.10.022; pmid: 34793707
20. C. Schneider *et al*., Tissue-resident group 2 innate lymphoid cells differentiate by layered ontogeny and in situ perinatal priming. *Immunity* **50**, 1425–1438.e5 (2019). doi: 10.1016/j.immuni.2019.04.019; pmid: 31128962
21. A. B. Molofsky, R. M. Locksley, The ins and outs of innate and adaptive type 2 immunity. *Immunity* **56**, 704–722 (2023). doi: 10.1016/j.immuni.2023.03.014; pmid: 37044061
22. T. Kobayashi *et al*., Homeostatic control of sebaceous glands by innate lymphoid cells regulates commensal bacteria equilibrium. *Cell* **176**, 982–997.e16 (2019). doi: 10.1016/j.cell.2018.12.031; pmid: 30712873
23. S. Saluzzo *et al*., First-breath-induced type 2 pathways shape the lung immune environment. *Cell Rep.* **18**, 1893–1905 (2017). doi: 10.1016/j.celrep.2017.01.071; pmid: 28228256
24. S. P. Gadani, I. Smirnov, A. T. Wiltbank, C. C. Overall, J. Kipnis, Characterization of meningeal type 2 innate lymphocytes and their response to CNS injury. *J. Exp. Med.* **214**, 285–296 (2017). doi: 10.1084/jem.20161982; pmid: 27994070
25. I. D. Vainchtein *et al*., Astrocyte-derived interleukin-33 promotes microglial synapse engulfment and neural circuit development. *Science* **359**, 1269–1273 (2018). doi: 10.1126/science.aal3589; pmid: 29420261
26. P. T. Nguyen *et al*., Microglial remodeling of the extracellular matrix promotes synapse plasticity. *Cell* **182**, 388–403.e15 (2020). doi: 10.1016/j.cell.2020.05.050; pmid: 32615087
27. R. T. Han *et al*., Microglial pattern recognition via IL-33 promotes synaptic refinement in developing corticothalamic circuits in mice. *J. Exp. Med.* **220**, e20220605 (2023). doi: 10.1084/jem.20220605; pmid: 36520518
28. D. He *et al*., Disruption of the IL-33-ST2-AKT signaling axis impairs neurodevelopment by inhibiting microglial metabolic adaptation and phagocytic function. *Immunity* **55**, 159–173.e9 (2022). doi: 10.1016/j.immuni.2021.12.001; pmid: 34982959
29. R. Rua, D. B. McGavern, Advances in meningeal immunity. *Trends Mol. Med.* **24**, 542–559 (2018). doi: 10.1016/j.molmed.2018.04.003; pmid: 29731353
30. K. Alves de Lima, J. Rustenhoven, J. Kipnis, Meningeal immunity and its function in maintenance of the central nervous system in health and disease. *Annu. Rev. Immunol.* **38**, 597–620 (2020). doi: 10.1146/annurev-immunol-102319-103410; pmid: 32340575
31. J. Wang, A. Rattner, J. Nathans, Bacterial meningitis in the early postnatal mouse studied at single-cell resolution. *eLife* **12**, e86130 (2023). doi: 10.7554/eLife.86130; pmid: 37318981
32. A. Zelco *et al*., Single-cell atlas reveals meningeal leukocyte heterogeneity in the developing mouse brain. *Genes Dev.* **35**, 1190–1207 (2021). doi: 10.1101/gad.348190.120; pmid: 34301765
33. I. Scheyltjens *et al*., Single-cell RNA and protein profiling of immune cells from the mouse brain and its border tissues. *Nat. Protoc.* **17**, 2354–2388 (2022). doi: 10.1038/s41596-022-00716-4; pmid: 35931780
34. D. Mrdjen *et al*., High-dimensional single-cell mapping of central nervous system immune cells reveals distinct myeloid subsets in health, aging, and disease. *Immunity* **48**, 380–395.e6 (2018). doi: 10.1016/j.immuni.2018.01.011; pmid: 29426702
35. H. Van Hove *et al*., A single-cell atlas of non-parenchymal brain macrophages reveals unique transcriptional identities that are shaped by ontogeny and tissue environment. *Nat. Neurosci.* **22**, 1021–1035 (2019). doi: 10.1038/s41593-019-0393-4; pmid: 31061494
36. R. T. Han *et al*., Interleukin-33 coordinates a microglial phagocytic response and limits corticothalamic excitability and seizure susceptibility. bioRxiv 2021.08.05.455250 [Preprint] (2021); https://doi.org/10.1101/2021.08.05.455250.
37. R. R. Ricardo-Gonzalez *et al*., Tissue signals imprint ILC2 identity with anticipatory function. *Nat. Immunol.* **19**, 1093–1099 (2018). doi: 10.1038/s41590-018-0201-4; pmid: 30201992
38. C. Schneider *et al*., A metabolite-triggered tuft cell-ILC2 circuit drives small intestinal remodeling. *Cell* **174**, 271–284.e14 (2018). doi: 10.1016/j.cell.2018.05.014; pmid: 29887373
39. S. J. Van Dyken *et al*., A tissue checkpoint regulates type 2 immunity. *Nat. Immunol.* **17**, 1381–1387 (2016). doi: 10.1038/ni.3582; pmid: 27749840
40. A. B. Molofsky *et al*., Innate lymphoid type 2 cells sustain visceral adipose tissue eosinophils and alternatively activated macrophages. *J. Exp. Med.* **210**, 535–549 (2013). doi: 10.1084/jem.20121964; pmid: 23420878
41. J. C. Nussbaum *et al*., Type 2 innate lymphoid cells control eosinophil homeostasis. *Nature* **502**, 245–248 (2013). doi: 10.1038/nature12526; pmid: 24037376
42. L. Lim, D. Mi, A. Llorca, O. Marín, Development and functional diversification of cortical interneurons. *Neuron* **100**, 294–313 (2018). doi: 10.1016/j.neuron.2018.10.009; pmid: 30359598
43. F. K. Wong *et al*., Pyramidal cell regulation of interneuron survival sculpts cortical networks. *Nature* **557**, 668–673 (2018). doi: 10.1038/s41586-018-0139-6; pmid: 29849154
44. M. W. Dahlgren *et al*., Adventitial stromal cells define group 2 innate lymphoid cell tissue niches. *Immunity* **50**, 707–722.e6 (2019). doi: 10.1016/j.immuni.2019.02.002; pmid: 30824323
45. K. M. Cautivo *et al*., Interferon gamma constrains type 2 lymphocyte niche boundaries during mixed inflammation. *Immunity* **55**, 254–271.e7 (2022). doi: 10.1016/j.immuni.2021.12.014; pmid: 35139352
46. R. Tremblay, S. Lee, B. Rudy, GABAergic interneurons in the neocortex: From cellular properties to circuits. *Neuron* **91**, 260–292 (2016). doi: 10.1016/j.neuron.2016.06.033; pmid: 27477017
47. S. J. Van Dyken, R. M. Locksley, Interleukin-4- and interleukin-13-mediated alternatively activated macrophages: Roles in homeostasis and disease. *Annu. Rev. Immunol.* **31**, 317–343 (2013). doi: 10.1146/annurev-immunol-032712-095906; pmid: 23298208
48. Z. Yao *et al*., A taxonomy of transcriptomic cell types across the isocortex and hippocampal formation. *Cell* **184**, 3222–3241.e26 (2021). doi: 10.1016/j.cell.2021.04.021; pmid: 34004146
49. L. C. Dorman *et al*., A type I interferon response defines a conserved microglial state required for effective neuronal phagocytosis. bioRxiv 2021.04.29.441889 [Preprint] (2022); https://doi.org/10.1101/2021.04.29.441889.
50. D. R. Herbert *et al*., Alternative macrophage activation is essential for survival during schistosomiasis and downmodulates T helper 1 responses and immunopathology. *Immunity* **20**, 623–635 (2004). doi: 10.1016/S1074-7613(04)00107-4; pmid: 15142530
51. A. Mo *et al*., Epigenomic signatures of neuronal diversity in the mammalian brain. *Neuron* **86**, 1369–1384 (2015). doi: 10.1016/j.neuron.2015.05.018; pmid: 26087164
52. S. Bugeon *et al*., A transcriptomic axis predicts state modulation of cortical interneurons. *Nature* **607**, 330–338 (2022). doi: 10.1038/s41586-022-04915-7; pmid: 35794483
53. A. F. Salvador, K. A. de Lima, J. Kipnis, Neuromodulation by the immune system: A focus on cytokines. *Nat. Rev. Immunol.* **21**, 526–541 (2021). doi: 10.1038/s41577-021-00508-z; pmid: 33649606
54. F. Zipp, S. Bittner, D. P. Schafer, Cytokines as emerging regulators of central nervous system synapses. *Immunity* **56**, 914–925 (2023). doi: 10.1016/j.immuni.2023.04.011; pmid: 37163992
55. O. Marín, Interneuron dysfunction in psychiatric disorders. *Nat. Rev. Neurosci.* **13**, 107–120 (2012). doi: 10.1038/nrn3155; pmid: 22251963

56. G. B. Choi *et al*., The maternal interleukin-17a pathway in mice promotes autism-like phenotypes in offspring. *Science* **351**, 933–939 (2016). doi: 10.1126/science.aad0314; pmid: 26822608
57. C. F. Vogelaar *et al*., Fast direct neuronal signaling via the IL-4 receptor as therapeutic target in neuroinflammation. *Sci. Transl. Med.* **10**, eaao2304 (2018). doi: 10.1126/scitranslmed.aao2304; pmid: 29491183
58. N. Hanuscheck *et al*., Interleukin-4 receptor signaling modulates neuronal network activity. *J. Exp. Med.* **219**, e20211887 (2022). doi: 10.1084/jem.20211887; pmid: 35587822
59. T. M. Brombacher *et al*., IL-4Rα deletion disrupts psychomotor performance and reference memory in mice while sparing behavioural phenotype associated with spatial learning. *Brain Behav. Immun.* **92**, 157–164 (2021). doi: 10.1016/j.bbi.2020.12.003; pmid: 33301870
60. S. Li *et al*., Interleukin-13 and its receptor are synaptic proteins involved in plasticity and neuroprotection. *Nat. Commun.* **14**, 200 (2023). doi: 10.1038/s41467-023-35806-8; pmid: 36639371
61. A. C. Yang *et al*., Physiological blood-brain transport is impaired with age by a shift in transcytosis. *Nature* **583**, 425–430 (2020). doi: 10.1038/s41586-020-2453-z; pmid: 32612231
62. J. A. Mazzitelli *et al*., Cerebrospinal fluid regulates skull bone marrow niches via direct access through dural channels. *Nat. Neurosci.* **25**, 555–560 (2022). doi: 10.1038/s41593-022-01029-1; pmid: 35301477
63. L. C. D. Smyth *et al*., Identification of direct connections between the dura and the brain. *Nature* **627**, 165–173 (2024). doi: 10.1038/s41586-023-06993-7; pmid: 38326613
64. S. D. Fernando, C. Rodrigo, S. Rajapakse, The 'hidden' burden of malaria: Cognitive impairment following infection. *Malar. J.* **9**, 366 (2010). doi: 10.1186/1475-2875-9-366; pmid: 21171998
65. M. Kasambala *et al*., Effect of *Schistosoma haematobium* infection on the cognitive functions of preschool age children and benefits of treatment from an endemic area in Zimbabwe. *BMC Infect. Dis.* **22**, 809 (2022). doi: 10.1186/s12879-022-07784-7; pmid: 36316647
66. T. Stuart *et al*., Comprehensive Integration of Single-Cell Data. *Cell* **177**, 1888–1902.e21 (2019). doi: 10.1016/j.cell.2019.05.031; pmid: 31178118

ACKNOWLEDGMENTS

We are grateful to the A.V.M. and A.B.M. labs, R. M. Locksley, and J. L. Rubenstein for helpful comments on the manuscript. We thank R. M. Locksley for sharing mouse strains, including *Il5*$^{Cre\text{-}RFP}$, *Il13*^{huCD4}, *Arg1*^{YFP}, *Ifng*^{YFP}, *R26*^{DTA}, *Il4ra*^{flox}, and *Il4ra*^{KO}; and M. Khierbeck, V. Sohal, and J. Crawley (UC Davis) for intellectual guidance and resources used for behavioral analyses. We thank M. Rosenberg, N. Silva, R. Cheng, S. Nelson, and J. Dennis for assistance with tissue preparation. We thank the University of California, San Franscisco (UCSF) Laboratory for Cell Analysis Core, the UCSF Parnassus Flow Core (RRID:SCR_018206 supported in part by grant NIH P30 DK063720 and by NIH S10 1S10OD021822-01), the UCSF Biological Imaging and Development Core, the UCSF Innovation Core at the Weill Institute, the UCSF Center for Advanced Light Microscopy, and the UCSF Laboratory Animal Resource Center for instruments and services. **Funding:** This work was supported by National Insistute for Mental Health (NIMH) Ruth L. Kirchstein Predoctoral National Research Service Award F31MH122207 (J.J.B.); the National Science Foundation Graduate Research Fellowships Program (S.E.T.); Vetenskapsrådet 2018-00307 (M.W.D.); National Institute of Allergy and Infectious Diseases (NIAID) T32 Training Grant 5T32AI007334 (C.C.E.); a Pew Scholars Award (A.V.M.); the Brain and Behavior Research Foundation (A.V.M.); National Institute of Neurological Disorders and Stroke (NINDS) 1R01NS126765 (A.V.M. and A.B.M.); NIMH R01MH125000 (A.V.M.); National Heart, Lung, and Blood Institute (NHLBI) 1R01HL142701 (A.B.M.); NIAID R01AI162806 (A.B.M.); NIAID R01AI180438 (A.B.M.); and NIMH R01MH125987 (K.J.B.). **Author contributions:** Conceptualization: J.J.B., A.V.M., A.B.M.; Methodology: J.J.B., N.M.M., M.W.D., A.V.M., A.B.M.; Investigation: J.J.B., N.M.M., S.E.T., M.W.D., J.F.O.-C., M.G.K., M.E.K., L.C.D., I.D.V., C.C.E., P.C.; Visualization: J.J.B., N.M.M., M.W.D., M.G.K., A.V.M., A.B.M.; Funding acquisition: J.J.B., A.V.M., A.B.M.; Project administration: A.V.M., A.B.M.; Supervision: A.V.M., A.B.M., K.J.B., T.J.N.; Writing – original draft: J.J.B., A.V.M., A.B.M.; Writing – review and editing: J.J.B., N.M.M., S.E.T., M.W.D., J.F.O.-C., L.C.D., I.D.V., C.C.E., P.C., M.G.K., A.V.M., A.B.M. **Competing interests:** The authors declare that they have no competing interests. **Data and materials availability:** All data needed to evaluate the conclusions in this paper are present in the paper or the supplementary materials. All mouse strains were obtained from Jackson Laboratories except for *Il4ra*$^{fl/fl}$, which was a gift from F. Brombacher, and are available from the authors upon request. scRNA-seq data and snRNA-seq data are available through Gene Expression Omnibus (GEO) accession nos. GSE236229 and GSE270237, respectively.

SUPPLEMENTARY MATERIALS

Submitted 8 April 2023; resubmitted 22 February 2024
Accepted 2 September 2024
10.1126/science.adi1025